



Cite this: *Phys. Chem. Chem. Phys.*, 2022, 24, 19783

## How change in chirality prevents $\beta$ -amyloid type interaction in a protonated cyclic dipeptide dimer<sup>†</sup>

Katia Le Barbu-Debus, Ariel Pérez-Mellor, ‡ Valéria Lepère and Anne Zehnacker \*

The protonated dimers of the diketopiperazine dipeptide cyclo (L-Phe-L-His) and cyclo (L-Phe-D-His) are studied by laser spectroscopy combined with mass spectrometry to shed light on the influence of stereochemistry on the clustering propensity of cyclic dipeptides. The marked spectroscopic differences experimentally observed in the hydride stretch region are well accounted for by the results of DFT calculations. Both diastereomeric protonated dimers involve a strong ionic hydrogen bond from the protonated imidazole ring of one monomer to the neutral imidazole nitrogen of the other. While this strong interaction is accompanied by a single NH···O hydrogen bond between the amide functions of the two moieties for the protonated dimer of cyclo (L-Phe-D-His), that of cyclo (L-Phe-L-His) involves two NH···O interactions, forming the motif of an antiparallel  $\beta$  sheet. Therefore, a change in chirality of the residue prevents the formation of the  $\beta$  sheet pattern observed in the amyloid type aggregation. These results emphasize the peculiar role of the histidine residue in peptide structure and interaction.

Received 8th July 2022,  
Accepted 5th August 2022

DOI: 10.1039/d2cp03110h

rsc.li/pccp

### Introduction

Peptide aggregation is associated with amyloid-related diseases such as Alzheimer's. The aggregation propensity depends on the environment, the amino-acid sequence (primary structure) and the protein secondary structure.<sup>1,2</sup> Although the cross- $\beta$  amyloid structure is the most frequently encountered pattern in the amyloid fibres, it was shown recently that other structures, including antiparallel  $\beta$  sheets, could play a role in the aggregation process.<sup>1,3,4</sup> Proteins and peptides involved in amyloidosis have been the subject of numerous *in vitro* studies using X-ray crystallography, electron diffraction, or NMR.<sup>1,2</sup> An alternative approach consists of studying short model peptides isolated in the gas phase to shed light on the factors that govern the non-covalent interactions (NCI) and, more precisely, the hydrogen bonds (HB) that control the molecular shape.<sup>5,6</sup> Neutral species have been studied under supersonic conditions by conformer-specific spectroscopy while room temperature or cryogenic ion trap studies shed light on the structure of protonated species or ion-core complexes.<sup>7–22</sup> Controlling the HB network by chemical design has paved the way to a wealth of interactions

and structures, not accessible to pure natural  $\alpha$  peptides. Original structures have emerged in  $\beta$  or  $\gamma$  peptides, or in artificial foldamers built from 2-amino cyclohexane carboxylic acid,<sup>23–29</sup> in which the bias introduced by the alicyclic ring results in stereochemical constraints that in turn modify the HB propensity.<sup>24</sup> The difference in HB propensity is observed for both intermolecular HB in the solid and intramolecular HB in jet-cooled monomers.<sup>26,30</sup> Introducing a heteroatom X in the ring stabilises intra-residues HB thanks to an additional NH···X interaction.<sup>31</sup> The conformational preference of small peptides is also modified by molecular interactions such as hydration,<sup>32</sup> or cluster formation.<sup>33</sup> Several studies have focused on the formation of  $\beta$ -sheets resulting in the aggregation of peptides. For example, capped phenylalanine-based peptides form dimers linked by  $\beta$ -sheet type NH···O interactions.<sup>10,34</sup>  $\beta$ -sheet formation was also observed in relatively large fragments of model amyloidogenic peptides. In addition,  $\beta$ -sheets were observed in oligomers of 6-residue fibril-forming peptide segments by combining ion mobility and IR spectroscopy.<sup>35</sup> The first steps of amyloid formation have been studied also in large systems under cryogenic ion trap conditions on the example of a model amyloidogenic peptide derived from the protein transthyretin.<sup>33</sup> However, less attention has been paid to the role of chirality in the aggregation of peptides. We focus here on the formation of protonated dimers of cyclo(Phe-His), a diketopiperazine-based cyclic dipeptide. This study aims to assess the influence of the chirality of the residues on the

*Institut des Sciences Moléculaires d'Orsay (ISMO), CNRS, Université Paris-Saclay, F-91405 Orsay, France. E-mail: anne.zehnacker-rentien@universite-paris-saclay.fr*

<sup>†</sup> Electronic supplementary information (ESI) available. See DOI: <https://doi.org/10.1039/d2cp03110h>

<sup>‡</sup> Current address: Department of Physical Chemistry, University of Geneva, 1211 Geneva, Switzerland.



formation of a  $\beta$ -sheet type interaction. The absolute configuration of the residues indeed influences the structure of cyclic dipeptides.<sup>36–41</sup> Cyclic dipeptides differ from linear ones in several aspects. First, the steric bias due to the ring imposes the non-usual *cis* conformation of the peptide bonds. It has been shown that amyloid-forming peptides contain amides with a *cis* conformation.<sup>42</sup> Cyclic dipeptides offer therefore a good model for studying the influence of the *cis* conformation of the peptide bond on aggregation. The *cis* conformation favours indeed the formation of two strong  $\text{NH}\cdots\text{O}$  hydrogen bonds in the gas-phase dimer of cyclo (Phe-Phe)<sup>43</sup> or its crystal,<sup>38,44</sup> akin to an antiparallel  $\beta$  sheet. Second, the molecule is deprived of the amine and carboxylic functions present in peptides, preventing protonation on the N-terminus. As a result, protonation of cyclic dipeptides usually happens on the amide CO, which results in the limited effect of chirality on their collision-induced dissociation (CID) efficiency.<sup>45–47</sup> Histidine-containing peptides stand out by the basic nature of the His residue, which is protonated on the imidazole ring.<sup>48</sup> This peculiar protonation site makes histidine very sensitive to solvation. The electronic spectrum recorded by UV photodissociation spectroscopy in a cryogenic ion trap shows a marked bathochromic shift relative to the aqueous solution.<sup>49</sup> Histidine also plays a particular role in the CID of peptides.<sup>50,51</sup> For example, doubly-charged peptides containing His at the N-terminus show enhanced backbone cleavage at the C-terminus relative to peptides with no His.<sup>52</sup> In contrast to peptides containing aliphatic residues, peptides containing histidine show diketopiperazine or lactam in addition to oxazolone fragments.<sup>51,53,54</sup> We recently showed that the CID of cyclo (Phe-His) $\text{H}^+$  shows a very high sensitivity of CO loss efficiency to the chirality of the residues, due to the proton shuttling mechanism from the imidazole substituent to the amide.<sup>45</sup> We determine here the structure of the protonated dimer of cyclo (*L*Phe-*L*His) and cyclo (*L*Phe-*D*His), noted in short (*c*-LL) $_2\text{H}^+$  and (*c*-LD) $_2\text{H}^+$ , in a room-temperature ion trap, by Infra-Red Multiple Photons Dissociation (IRMPD) and compare them to quantum chemical calculations in the frame of the density functional theory (DFT). We aim to evidence how a change in the absolute configuration of the residue makes it possible or not to form a  $\beta$ -sheet type interaction between the two peptides.

## Experimental and theoretical methods

### (a) Nomenclature

The structure of the protonated cyclo (Phe-His) monomer is shown in Chart 1. The nomenclature and numbering of atoms are those used previously.<sup>45</sup> In short, each aromatic ring may adopt one of the three following orientations, defined by the dihedral angles  $\tau$ (NCCC), namely, two gauche and one trans forms, denoted as  $g^+$ ,  $g^-$  and  $t$ , respectively.  $g^+$ ,  $g^-$  and  $t$  correspond to  $\tau$ (NCCC) of around  $60^\circ$ ,  $-60^\circ$  and  $180^\circ$ , respectively, for the *L* residue, with opposite values for the *D* residue. In a  $g^+$  structure, the aromatic substituent is folded over the DPK ring while it is extended outwards in  $g^-$ .<sup>38,55</sup> The trans geometry also corresponds to an extended aromatic ring, but with its plane almost perpendicular to the DPK ring. In addition, the two nitrogen atoms of the imidazole ring are named according to the IUPAC Compendium of Chemical Terminology, as proposed for  $\text{HisH}^+$ .<sup>48</sup> The nitrogen atom close to the peptide ring is denoted by  $\text{N}_\pi$ , while the farthest one is called  $\text{N}_\tau$ , as depicted in Chart 1. The neutral monomer exists in two tautomeric forms shown in Chart 1, namely, the  $\text{N}_\pi\text{H}$  or  $\text{N}_\tau\text{H}$  tautomer depending on the location of the hydrogen. The two entities of the protonated dimer are differentiated by their charge state. The atoms belonging to the protonated moiety will be denoted by “P” in subscript, while those of the neutral moiety will be denoted by “N”. For example, the carbon  $\text{C}_1$  of the neutral part will be denoted  $\text{C}_{\text{N}1}$  and the nitrogen  $\text{N}_\pi$  of the protonated part will be called  $\text{N}_{\text{P}\pi}$ .

### (b) Experimental methods

Tandem mass spectrometry experiments were performed in the room temperature 7T FT-ICR hybrid mass spectrometer (Bruker, Apex Qe) equipped with an Apollo II electrospray ionization source of the SMAS (Spectrométrie de Masse, Analyse et Spectroscopie) facility at the Centre Laser Infrarouge d'Orsay (CLIO).<sup>56–58</sup> The protonated dimers were generated by electrospray of slightly acidified 50  $\mu\text{M}$  solutions in a 50:50 mixture of methanol and water. The dipeptides were obtained from Novopep (China) (98% purity). The details of the experiments can be found in previous publications.<sup>45,46,59–61</sup> Briefly, the ions were mass-selected in a quadrupole mass filter, thermalized in

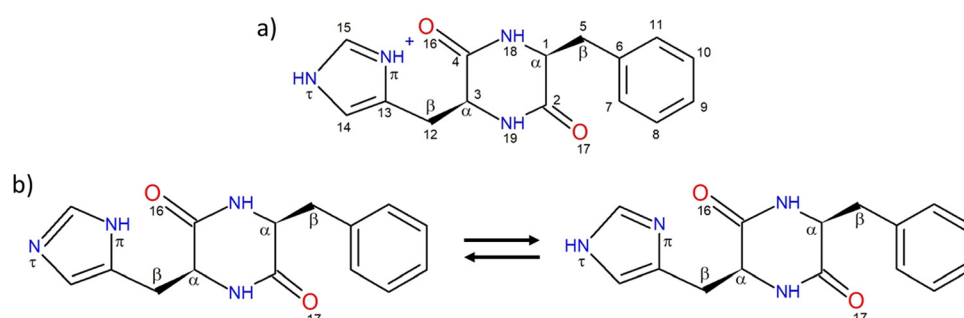


Chart 1 (a) Structure of protonated cyclo *L*Phe-*L*His and numbering of the atoms. (b) Structure of the  $\text{N}_\pi\text{H}$ -tautomer (left) and  $\text{N}_\tau\text{H}$ -tautomer (right) of neutral cyclo *L*Phe-*L*His.



the hexapole linear trap by colliding with argon, and transferred to the FT-ICR cell.

Vibrational spectra were obtained by means of Infrared Multiple Photon Dissociation (IRMPD).<sup>62</sup> The IRMPD spectra were obtained by irradiating the mass-selected and thermalized ions in the ICR cell and monitoring the  $\ln$  of the total fragmentation efficiency  $\Phi = -\ln(P/(F + P))$  as a function of the IR wavelength, with  $P$  and  $F$  being the abundance of the parent and the sum of the fragments, respectively. The spectra were recorded in the fingerprint region (800–1800  $\text{cm}^{-1}$  region) by mildly focusing the CLIO free-electron laser (FEL) (25 Hz repetition rate) by a 2000 mm Ag-protected spherical mirror to a beam diameter of  $\sim 1$  mm at the interaction zone.<sup>57</sup> The spectral bandwidth (full width at half-maximum FWHM) was about 7  $\text{cm}^{-1}$ , with a power of 1.6 to 1 W from 800 to 1800  $\text{cm}^{-1}$ . For the 3  $\mu\text{m}$  spectral region, an IR Optical Parametric Oscillator (LaserVision OPO, 5–10 mJ pulse<sup>-1</sup>) was slightly focused by the same spherical mirror. The irradiation time was carefully adjusted to avoid the saturation of the most intense transitions. No collisional cooling could occur between two laser pulses during the irradiation of the ions in the FT-ICR cell due to the very low pressure there ( $<10^{-9}$  mbar).

### (c) Computational methods

The potential energy surface (PES) was explored using the Monte-Carlo Multiple Minima procedure in the MacroModel suite and the Maestro interface of the Schrödinger package.<sup>63</sup> For each protonated dimer  $(\text{c-LL})_2\text{H}^+$  and  $(\text{c-LD})_2\text{H}^+$ , the two tautomers of the neutral moiety, namely,  $\text{N}_\pi\text{H}$  and  $\text{N}_\tau\text{H}$ , were considered. Two protonation sites were also considered, setting a formal charge +1 on  $\text{N}_\pi\text{H}^+$  or  $\text{N}_\tau\text{H}^+$ . Five simulations, using different sampling methods of the “advanced conformational search” option and the OPLS2005 force field,<sup>64</sup> were performed for each structure. The window in energy was fixed to 10 kcal mol<sup>-1</sup>. The number of isomers was then reduced using the “redundant option” included in Macromodel program. The used root-mean-square deviation was chosen so that between 60 and 80 conformers were obtained at the end of the process, for the different explorations.

All the geometries obtained at this stage were fully optimized in the gas phase in the frame of the density functional theory (DFT) using the TURBOMOLE package.<sup>65,66</sup> The calculations were performed with the b97-d functional including dispersion corrections<sup>67,68</sup> and the TZVPP basis set,<sup>69</sup> which is a good compromise between accuracy and calculation time for systems of this size with a large number of isomers. The resolution of the identity was used to reduce the computation time.<sup>70</sup> All minima beyond 5 kcal mol<sup>-1</sup> were then re-optimised at the ri-b97-d-D3BJ/def2-TZVPPD level of theory.<sup>68,71</sup> The calculations were performed in both the gas phase and solution. Solvation was accounted for by the “cosmo” keyword, using a dielectric constant of water  $\epsilon = 80$ , to reproduce the conditions of an aqueous solution prior to the electrospray. The harmonic frequencies were calculated at the same level of theory and scaled by a factor of 0.978 to account for basis set incompleteness and anharmonicity. The spectra were simulated by convoluting

the scaled harmonic frequencies by a Gaussian line shape of 10  $\text{cm}^{-1}$  FWMH. In what follows, we give the energies corrected by the zero-point-energy (ZPE) at 0 K in vacuum ( $\Delta E$ ) as well as the Gibbs free energies at room temperature in vacuum ( $\Delta G$ ) and in solution ( $\Delta G_{\text{sol}}$ ). The complexes retained for the assignment were re-optimised using the B3LYP functional with D3 dispersion corrections and the 6-311++G(d,p) basis sets,<sup>71–74</sup> using the Gaussian16 B01 software.<sup>75</sup> The frequencies were calculated at the same level of theory and scaled by 0.955 as for the monomer. The results are identical to those discussed here and are shown in Fig. S1 of the ESI,<sup>†</sup> for the 3  $\mu\text{m}$  region.

## Results and discussion

### (a) Experimental results

The vibrational spectrum of the  $(\text{c-LL})_2\text{H}^+$  and  $(\text{c-LD})_2\text{H}^+$  protonated dimers have been recorded in both the fingerprint and the OH/NH/CH stretch region by monitoring the fragment at  $m/z$  284, *i.e.* the protonated monomer, which is the only fragment observed by CID. The fingerprint region is identical for the two diastereomers and will be discussed later. In contrast, the 3000–3600  $\text{cm}^{-1}$  region shows striking differences between  $(\text{c-LL})_2\text{H}^+$  and  $(\text{c-LD})_2\text{H}^+$ , as shown in Fig. 1.

The major difference between the  $(\text{c-LL})_2\text{H}^+$  and  $(\text{c-LD})_2\text{H}^+$  protonated dimers is the presence of two intense transitions located at 3385 and 3418  $\text{cm}^{-1}$  for  $(\text{c-LD})_2\text{H}^+$ , which contrasts with the single intense feature observed for  $(\text{c-LL})_2\text{H}^+$  at 3422  $\text{cm}^{-1}$ . The other transitions in this region are similar for the two diastereomers, with a weak band at 3500  $\text{cm}^{-1}$  and three broad bands in the low-frequency range, at 3225, 3155 and 3090  $\text{cm}^{-1}$ . The broad transition observed at  $\sim 3230$   $\text{cm}^{-1}$  also has larger relative intensity and a different shape in  $(\text{c-LD})_2\text{H}^+$  compared to  $(\text{c-LL})_2\text{H}^+$ .

### (b) Calculated structures and assignment

The spectra of all calculated structures were compared to the experiment by visual examination. The simulated spectra showing the best match with the experiment are shown in Fig. 1. The corresponding calculated structures are given in Fig. 2 and the most relevant structural parameters are listed in Table 1.

Only one structure among those calculated accounts for the spectrum of  $(\text{c-LD})_2\text{H}^+$ , namely  $\pi$ -(c-LD)<sub>2</sub>H<sup>+</sup> (see Fig. 2a). In contrast, the spectrum of  $(\text{c-LL})_2\text{H}^+$  can be simulated using any of the calculated  $(\text{c-LL})_2\text{H}^+$  structures shown in Fig. 2b and c, namely,  $\pi$ -(c-LL)<sub>2</sub>H<sup>+</sup> and  $\tau$ -(c-LL)<sub>2</sub>H<sup>+</sup>. It should be noticed that none of the calculated structures accounting for the experimental results is the most stable protonated dimer. In terms of  $\Delta E$ ,  $\pi$ -(c-LL)<sub>2</sub>H<sup>+</sup> or  $\tau$ -(c-LL)<sub>2</sub>H<sup>+</sup> are indeed destabilised by 3.4 and 4.0 kcal mol<sup>-1</sup>, respectively, relative to the most stable calculated form, and  $\pi$ -(c-LD)<sub>2</sub>H<sup>+</sup> by 1.1 kcal mol<sup>-1</sup>. A similar situation is encountered for  $\Delta G$  with  $\pi$ -(c-LL)<sub>2</sub>H<sup>+</sup> or  $\tau$ -(c-LL)<sub>2</sub>H<sup>+</sup> destabilised by 3.7 kcal mol<sup>-1</sup> and  $\pi$ -(c-LD)<sub>2</sub>H<sup>+</sup> by 2.0 kcal mol<sup>-1</sup>. Solvation does not substantially modify the energetics and  $\Delta G_{\text{sol}}$  amounts to 6.3 and 6.2 kcal mol<sup>-1</sup> for  $\pi$ -(c-LL)<sub>2</sub>H<sup>+</sup> or  $\tau$ -(c-LL)<sub>2</sub>H<sup>+</sup>,



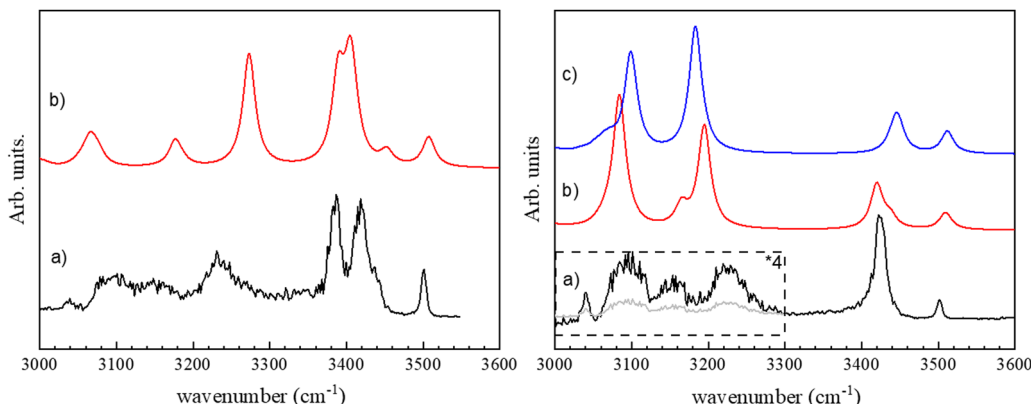


**Fig. 1** Left: (a) Experimental IRMPD spectrum of  $c\text{-(LD)}_2\text{H}^+$  in the region of  $3\ \mu\text{m}$ . (b) Simulated spectrum for  $\pi\text{-(c-LD)}_2\text{H}^+$ . Right: (a) Experimental IRMPD spectrum of  $c\text{-(LL)}_2\text{H}^+$ . (b) Simulated spectrum for  $\pi\text{-(c-LL)}_2\text{H}^+$ . (c) Simulated spectrum for  $\tau\text{-(c-LL)}_2\text{H}^+$  (see text).

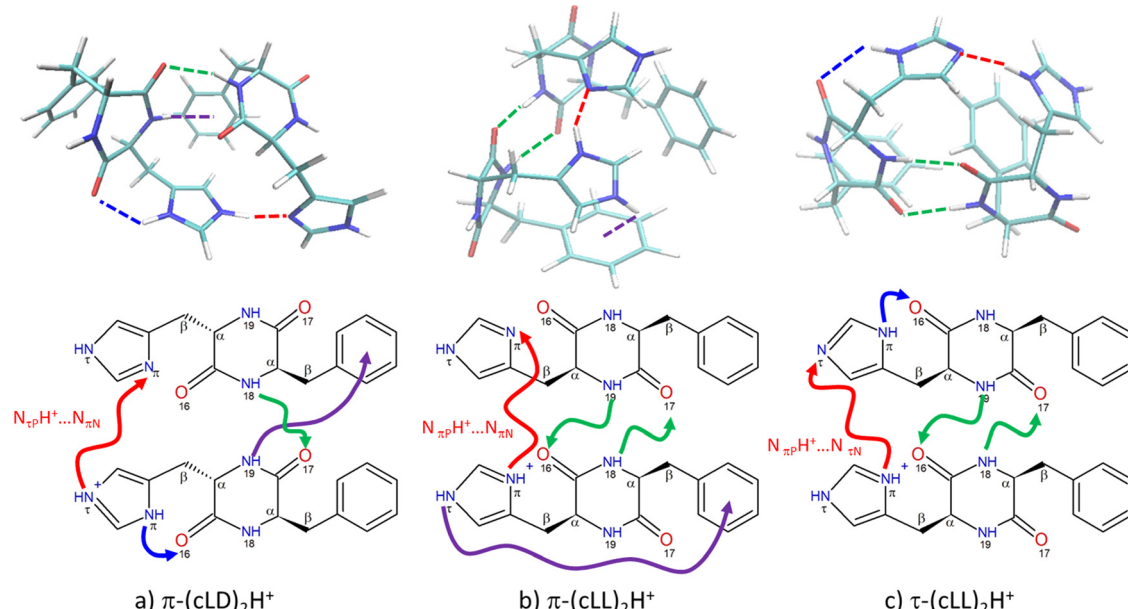


**Fig. 2** Protonated dimers accounting for the experimental spectrum, calculated at the ri-b97-d-D3BJ/def2-TZVPPD level of theory. (a)  $\pi\text{-(c-LD)}_2\text{H}^+$ , (b)  $\pi\text{-(c-LL)}_2\text{H}^+$ , and (c)  $\tau\text{-(c-LL)}_2\text{H}^+$ . Hydrogen bonds are indicated by dashed lines in the 3D structures (top) and by arrows in the 2D schemes (bottom). The strong ionic  $\text{NH}^+ \cdots \text{N}$  interaction is shown in red, the neutral  $\text{NH} \cdots \text{O}$  interactions in green, the  $\text{NH} \cdots \pi$  interactions in purple, and the intramolecular  $\text{NH} \cdots \text{O}$  interaction in blue.

respectively, and  $2.6\ \text{kcal mol}^{-1}$  for  $\pi\text{-(c-LD)}_2\text{H}^+$ . We can conclude from these values that solvation does not favour the observed complexes, but an increase in temperature does. It is therefore possible that high temperature and transient conditions during the electro-spray ionisation process are responsible for the observed structures. Still, the assignment is unambiguous due to the excellent match between simulated and observed spectra. The spectrum of the most stable calculated protonated dimer does not match the experiment and is shown in Fig. S2 of the ESI.†

The proton is located on the imidazole ring in all the calculated structures, whether  $(c\text{-LL})_2\text{H}^+$  or  $(c\text{-LD})_2\text{H}^+$ . This is identical to what has been observed in the protonated histidine monomer or its complexes<sup>48,76</sup> and in the protonated cyclo-

(Phe-His) monomer.<sup>45,49</sup> Moreover, the phenyl ring of Phe is always folded over the DPK ring ( $g^+$  geometry) for  $(c\text{-LL})_2\text{H}^+$  and  $(c\text{-LD})_2\text{H}^+$  alike and whether the subunit within the dimer is neutral or protonated. The histidine aromatic ring of the protonated moiety is also folded on the aromatic ring ( $g^+$  geometry). This contrasts with the protonated monomers, shown in Fig. S3 of the ESI,† in which His is in  $t$  geometry to allow the formation of the intramolecular  $\text{NH}^+ \cdots \text{O}$  hydrogen bond. The latter is broken in the dimer to the benefit of the strong intermolecular ionic  $\text{NH}^+ \cdots \text{N}$  interaction. The histidine aromatic ring of the neutral moiety is also  $g^+$  in both  $(c\text{-LL})_2\text{H}^+$  calculated conformers. The folded conformation of all the aromatic ring results in very compact structures that allow maximising the hydrogen bonds and optimising the dispersion.



**Table 1** Structural parameters defining the structures of  $\pi$ -(c-LD)<sub>2</sub>H<sup>+</sup> and  $\tau$ -(c-LL)<sub>2</sub>H<sup>+</sup>. The dihedral angles are defined as  $\tau_1(N_{18}C_1C_5C_6)$  and  $\tau_2(N_{19}C_3C_{12}C_{13})$ . The first letter in the Newman projection thus corresponds to the Phe residue (always L), and the second letter to His (L or D). The interactions are characterized by the hydrogen bond length or the inter-ring distance and the angle defining the linearity of the hydrogen bond, given in parentheses

Structure	Charge state of monomers	Newman projection	$\tau_1$ (°)	$\tau_2$ (°)	Distance between the centres of the aromatic rings (Å)	Intramolecular interaction	Intermolecular interaction
$\pi$ -(cLD) <sub>2</sub> H <sup>+</sup>	Neutral (N)	$g_D^+g_L^-$	-54	-73	6.91	$C_{N3}H \cdots \pi_{NPhe}$ (3.82 Å) $N_{N19}H \cdots \pi_{NHis}$ (3.42 Å) $C_{P32}H \cdots \pi_{PPhe}$ (2.50 Å) $N_{P\pi}H \cdots O_{P16}$ (2.10 Å)	$N_{P19}H \cdots \pi_{NPhe}$ (2.91 Å) $N_{N18}H \cdots O_{P17}C$ (1.96 Å; 160°) $N_{P\tau}H^+ \cdots N_{N\pi}$ (1.68 Å; 168°)
	Protonated (P)	$g_D^+g_L^+$	-63	62	7.03		
$\pi$ -(cLL) <sub>2</sub> H <sup>+</sup>	Neutral (N)	$g_L^+g_L^+$	72	65	4.50	$\pi_{NPhe} \cdots \pi_{NHis}$ (4.50 Å)	$N_{N19}H \cdots O_{P16}$ (1.77 Å; 175°) $N_{P18}H \cdots O_{N17}$ (1.97 Å; 161°) $N_{P\pi}H^+ \cdots N_{N\pi}$ (1.72 Å; 156°)
	Protonated (P)	$g_L^+g_L^+$	66	73	3.87	$\pi_{PPhe} \cdots \pi_{PHis}$ (3.87 Å)	
$\tau$ -(cLL) <sub>2</sub> H <sup>+</sup>	Neutral (N)	$g_L^+g_L^+$	50	54	6.75	$N_{N\pi} \cdots O_{N16}$ (2.20 Å)	$N_{N19}H \cdots O_{P16}$ (1.96 Å; 171°) $N_{P18}H \cdots O_{N17}$ (1.82 Å, 172°) $N_{P\pi}H^+ \cdots N_{N\pi}$ (1.68 Å; 166°)
	Protonated (P)	$g_L^+g_L^+$	61	51	3.64	$\pi_{PPhe} \cdots \pi_{PHis}$ (3.87 Å)	

$\pi$ -(c-LD)<sub>2</sub>H<sup>+</sup> stands out by the  $g^-$  conformation of the His aromatic substituent. This results in a less compact geometry, with an extended imidazole conformation of the imidazole ring that is necessary for the concomitant formation of the ionic  $N_{P\pi}H^+ \cdots N_{N\pi}$  interaction and the  $N_{P\pi}H \cdots O_{N16}$  hydrogen bridge.

As seen in Fig. 2, the (c-LL)<sub>2</sub>H<sup>+</sup> and (c-LD)<sub>2</sub>H<sup>+</sup> dimers have in common a strong ionic intermolecular hydrogen bond  $NH^+ \cdots N$  linking the two moieties. (c-LL)<sub>2</sub>H<sup>+</sup> and (c-LD)<sub>2</sub>H<sup>+</sup> differ by the location of the NH involved in the ionic hydrogen bond, on  $N_\tau$  for (c-LD)<sub>2</sub>H<sup>+</sup> and  $N_\pi$  for (c-LL)<sub>2</sub>H<sup>+</sup>. Notwithstanding this difference, the characteristics of the ionic hydrogen bond are similar in all the structures shown in Fig. 2. Although strong, this hydrogen bond cannot be seen as a completely shared proton. The NH bond length is indeed of the order of 1.07 Å vs. ~1.7 Å for the  $NH^+ \cdots N$  distance. The hydrogen bond is not far from linearity (~155–170°). In all cases, NBO calculations indicate that the positive charge is mostly localized (~0.65) on the NH involved in the ionic hydrogen bond. The neutral moiety corresponds to a different tautomer for the different calculated dimers.  $\pi$ -(c-LD)<sub>2</sub>H<sup>+</sup> or  $\pi$ -(c-LL)<sub>2</sub>H<sup>+</sup> contain the most stable neutral  $N_\pi H$  tautomer, whose structure has been determined by rotational spectroscopy in the gas phase.<sup>77</sup> In  $\tau$ -(c-LL)<sub>2</sub>H<sup>+</sup>, it is the less stable  $N_\tau H$  tautomer, akin to the 5-imidazole tautomer.

The most striking difference between (c-LL)<sub>2</sub>H<sup>+</sup> and (c-LD)<sub>2</sub>H<sup>+</sup> is the pattern of the additional hydrogen bonds that stabilise the dimer. In  $\pi$ -(c-LD)<sub>2</sub>H<sup>+</sup>, a single additional neutral  $N_{N18}H \cdots O_{P17}$  intermolecular hydrogen bond is formed between the two peptide rings, bridging the amide NH of the neutral Phe residue to the amide CO of the protonated Phe residue. An additional  $N_{P\pi}H \cdots O_{P16}$  intramolecular interaction within the protonated moiety is also present, reminiscent of what is observed in the protonated monomer.<sup>45</sup> In addition,  $N_{19p}H$  forms a weak  $NH \cdots \pi$  hydrogen bond with the benzene ring of the neutral moiety.

In contrast, the (c-LL)<sub>2</sub>H<sup>+</sup> dimers accounting for the experimental spectrum involve two  $NH \cdots OC$  hydrogen bonds. This pattern has been observed in the solid state of cyclo (Phe–Phe) or its dimer under supersonic expansion conditions.<sup>78</sup> The two dimers, namely,  $\pi$ -(c-LL)<sub>2</sub>H<sup>+</sup> and  $\tau$ -(c-LL)<sub>2</sub>H<sup>+</sup> have very similar

structures. They both show the major ionic  $N_{P\pi}H^+ \cdots N$  interaction described above. However, they differ in the tautomer of the neutral subunit acting as an acceptor in this intermolecular H bond. For  $\pi$ -(c-LL)<sub>2</sub>H<sup>+</sup>, the acceptor nitrogen is  $N_{N\pi}$ , as observed in (c-LD)<sub>2</sub>H<sup>+</sup>, while for  $\tau$ -(c-LL)<sub>2</sub>H<sup>+</sup> it is  $N_{N\tau}$ . In both  $\pi$ -(c-LL)<sub>2</sub>H<sup>+</sup> and  $\tau$ -(c-LL)<sub>2</sub>H<sup>+</sup>, the two peptide rings are linked by two head-to-head  $NH \cdots O$  hydrogen bonds, forming an anti-parallel  $\beta$ -sheet pattern. For  $\pi$ -(c-LL)<sub>2</sub>H<sup>+</sup> and  $\tau$ -(c-LL)<sub>2</sub>H<sup>+</sup> alike, one of the  $NH \cdots OC$  bonds is formed from the phenylalanine NH group of the protonated moiety to the phenylalanine CO group of the neutral. The other  $NH \cdots OC$  bonds is formed from the histidine NH group of the neutral moiety to the histidine CO group of the protonated part.

We can now assign the experimental spectra at the light of the structures described above. The experimental spectrum of (c-LD)<sub>2</sub>H<sup>+</sup> (see Fig. 1a) can be safely assigned to  $\pi$ -(c-LD)<sub>2</sub>H<sup>+</sup>. The medium intensity transition observed at 3500 cm<sup>-1</sup> is assigned to the neutral imidazole  $\nu(N_{N\tau}H)$  calculated at 3508 cm<sup>-1</sup>. The free  $\nu(N_\tau H)$  in histidine-containing peptides also appears in the same range between 3500 and 3520 cm<sup>-1</sup>.<sup>79</sup> The  $\nu(NH)$  frequency observed here is similar but slightly lower than the free  $\nu(NH)$  frequency of imidazole trapped in helium droplets (3517.8 cm<sup>-1</sup>),<sup>80</sup> in jet-cooled imidazole complexes (3515–3520 cm<sup>-1</sup>) or imidazole containing peptides.<sup>79,81,82</sup>

The intense experimental doublet at 3385 and 3418 cm<sup>-1</sup> is well reproduced by the simulations. The higher-energy transition of the doublet is assigned to the  $N_{P\pi}H^+$  vibration of the protonated imidazole that gains intensity through the intramolecular  $NH \cdots O$  interaction. The lower-energy component of the doublet is assigned to the amide  $\nu(N_{P19}H)$  of the histidine residue of the protonated sub-unit, which gains intensity due to the  $NH \cdots \pi$  intermolecular interaction with the benzene ring of the neutral sub-unit. The shoulder on the high-energy side of the doublet at 3437 cm<sup>-1</sup> is assigned to a free amide  $\nu(N_{P18}H)$ . The broad band at 3233 cm<sup>-1</sup> is attributed to the amide  $\nu(N_{N18}H)$  of the phenylalanine residue involved in the intermolecular  $N_{N18}H \cdots O_{P17}H$  bond, calculated at 3274 cm<sup>-1</sup>. Its intensity is weaker in the experiment than in the simulation because of the low energy of the laser in this range and the



band broadening resulting from the strong HB formation. The very weak features below  $3200\text{ cm}^{-1}$  are due to  $\nu(\text{CH})$  stretches. The frequency of the protonated imidazole  $\nu(\text{N}_{\text{P}_\tau}\text{H}^+)$  involved in the intermolecular  $\text{N}_{\text{P}_\tau}\text{H}^+\cdots\text{N}_{\text{N}_\pi}$  hydrogen bond is calculated at  $2454\text{ cm}^{-1}$  due to its ionic character and is out of the wavelength range of the IR OPO used as a light source. Last, the weak and broad absorption bands at  $\sim 3180$  and  $3050\text{ cm}^{-1}$  are due to the aromatic  $\nu(\text{CH})$  of the imidazole and phenyl moieties, respectively.

The calculated spectra of  $\pi\text{-}(\text{c-LL})_2\text{H}^+$  and  $\tau\text{-}(\text{c-LL})_2\text{H}^+$  are very similar in the hydride stretch region. We shall first compare the experimental spectrum to that simulated for  $\pi\text{-}(\text{c-LL})_2\text{H}^+$ . The experimental band at  $3501\text{ cm}^{-1}$  corresponds to  $\nu(\text{N}_{\text{N}_\pi}\text{H})$  of the neutral imidazole calculated at  $3510\text{ cm}^{-1}$ , similarly to  $(\text{c-LD})_2\text{H}^+$ . The single intense band at  $3424\text{ cm}^{-1}$  is attributed to  $\nu(\text{N}_{\text{P}_\tau}\text{H})$  of the protonated imidazole, whose frequency is downshifted and intensity is increased due to  $\text{NH}\cdots\pi$  intramolecular interaction with the phenylalanine aromatic ring. The observed frequency is slightly lower than that observed in the imidazole/benzene complex ( $3445\text{ cm}^{-1}$ ), which also involves an  $\text{NH}\cdots\pi$  interaction,<sup>83</sup> probably because of a partial delocalisation of the positive charge in the imidazole ring. The two experimental broad bands at  $3224$  and  $3092\text{ cm}^{-1}$  are assigned to the two amide  $\nu(\text{NH})$  involved in the  $\beta$ -sheet pattern. The vibrational modes calculated at  $3084$  and  $3196\text{ cm}^{-1}$  are mainly localised on the  $\text{N}_{\text{N}_{19}}\text{H}$  of the neutral moiety and  $\text{N}_{\text{P}_{18}}\text{H}$  of the protonated moiety, respectively. This is reminiscent of what is observed in the solid-state of DKP dipeptides. Crystallographic results unambiguously show the presence of antiparallel  $\beta$ -sheets with two different  $\text{NH}\cdots\text{O}$  distances, even in symmetrical systems like cyclo (Phe–Phe), resulting in two different frequencies. The shoulders at  $3170\text{ cm}^{-1}$  that appear in the same range in the calculated spectrum are due to imidazole  $\nu(\text{CH})$ . The frequency of the  $\text{N}_\pi\text{H}^+$  involved in the ionic intermolecular hydrogen bond, calculated at  $2590\text{ cm}^{-1}$ , cannot be observed experimentally as it was the case for  $(\text{c-LD})_2\text{H}^+$ .

Comparing the experimental spectrum to  $\tau\text{-}(\text{c-LL})_2\text{H}^+$  leads to the following assignment: the experimental band at

$3501\text{ cm}^{-1}$  is associated with the transition calculated at  $3510\text{ cm}^{-1}$  corresponding to the  $\nu(\text{N}_{\text{P}_\tau}\text{H})$  of the protonated imidazole, a value close to that observed in protonated histidine ( $3482\text{ cm}^{-1}$ ).<sup>49</sup> The intense band at  $3424\text{ cm}^{-1}$  is attributed to  $\nu(\text{N}_{\text{N}_\pi}\text{H})$  of the neutral imidazole calculated at  $3445\text{ cm}^{-1}$ . The transition is shifted down in frequency and gains intensity relative to its counterpart in  $\pi\text{-}(\text{c-LL})_2\text{H}^+$  due to an intramolecular  $\text{N}_{\text{N}_\pi}\text{H}\cdots\text{O}_{\text{N}_{16}}$  interaction. It should be underlined that the  $\text{N}_{\text{N}_\pi}\text{H}\cdots\text{O}_{\text{N}_{16}}$  interaction is only possible for  $\tau\text{-}(\text{c-LL})_2\text{H}^+$  but not in  $\pi\text{-}(\text{c-LL})_2\text{H}^+$  because  $\text{N}_{\text{N}_\pi}\text{H}$  is too far from the HB donor. Finally, the two broad experimental bands at  $3224$  and  $3092\text{ cm}^{-1}$  correspond to the two intense calculated transitions at  $3099$  and  $3183\text{ cm}^{-1}$ . They stem from the amide  $\nu(\text{NH})$  involved in the intermolecular  $\text{NH}\cdots\text{O}$  hydrogen bonds. As observed in  $\pi\text{-}(\text{c-LL})_2\text{H}^+$ , the two bonded amide  $\nu(\text{NH})$  are localized in  $\tau\text{-}(\text{c-LL})_2\text{H}^+$ . Their frequency order is inverted relative to  $\pi\text{-}(\text{c-LL})_2\text{H}^+$ . The  $\nu(\text{N}_{\text{P}_{18}}\text{H})$  located on  $\text{N}_{\text{P}_{18}}\text{H}\cdots\text{O}_{\text{N}_{17}}$  is now lower in frequency, reflecting an inversion in the  $\text{NH}\cdots\text{O}$  distances (see Table 1). As described for  $(\text{c-LD})_2\text{H}^+$ , the  $\nu(\text{CH})$  appear in the same range and are responsible for the experimental shoulder at  $3090\text{ cm}^{-1}$ . The frequency of the  $\text{N}_{\text{P}_\pi}\text{H}^+$  involved in the ionic intermolecular hydrogen bond is calculated at  $2521\text{ cm}^{-1}$  and cannot be experimentally observed, it is slightly lower in frequency than  $\pi\text{-}(\text{c-LL})_2\text{H}^+$ .

The experimental spectrum in the  $3\text{ }\mu\text{m}$  region does not allow assigning unambiguously the observed protonated  $(\text{c-LL})_2\text{H}^+$  dimer to  $\pi\text{-}(\text{c-LL})_2\text{H}^+$  or  $\tau\text{-}(\text{c-LL})_2\text{H}^+$ . We cannot make the assignment based on relative energies as both protonated  $(\text{c-LL})_2\text{H}^+$  dimers have similar Gibbs energy. Therefore, we have also recorded the IRMPD spectrum in the fingerprint region. It is shown in Fig. 3 together with the calculated spectra of  $\pi\text{-}(\text{c-LL})_2\text{H}^+$  and  $\tau\text{-}(\text{c-LL})_2\text{H}^+$ . In contrast to the  $3\text{ }\mu\text{m}$  region, the calculated fingerprint region show spectral differences, allowing us to preferentially assign the observed complex to  $\pi\text{-}(\text{c-LL})_2\text{H}^+$ . Indeed, the transitions observed at  $1422$  and  $1327\text{ cm}^{-1}$  are better accounted for by the calculated spectrum of  $\pi\text{-}(\text{c-LL})_2\text{H}^+$ . Moreover, the calculated transition at  $1080\text{ cm}^{-1}$  and the shoulder at  $1620\text{ cm}^{-1}$  seem to be experimentally observed at  $1090\text{ cm}^{-1}$  and  $1620\text{ cm}^{-1}$ , respectively. It should

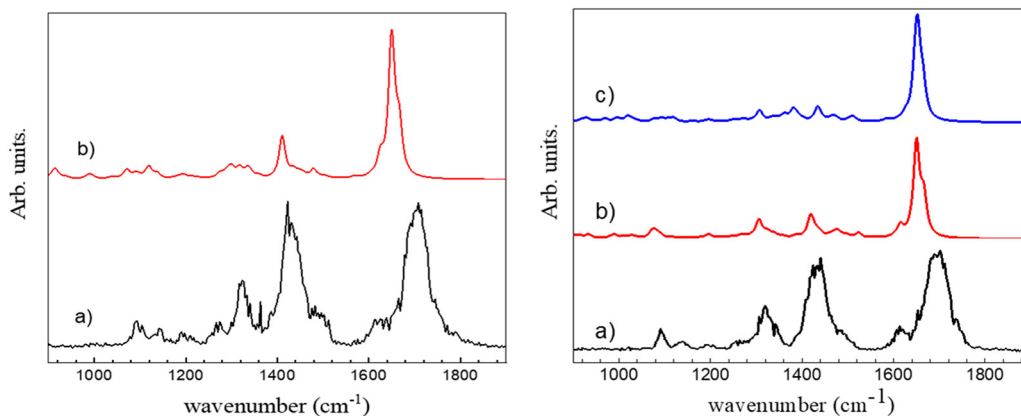


Fig. 3 Left: (a) Experimental IRMPD spectrum of  $\text{c-(LD)}_2\text{H}^+$  in the fingerprint region. (b) Simulated spectrum for  $\pi\text{-}(\text{c-LD})_2\text{H}^+$ . Right: (a) Experimental IRMPD spectrum of  $\text{c-(LL)}_2\text{H}^+$  in the fingerprint region. (b) Simulated spectrum for  $\pi\text{-}(\text{c-LL})_2\text{H}^+$ . (c) Simulated spectrum for  $\tau\text{-}(\text{c-LL})_2\text{H}^+$ .



be noted that the triplet observed in the amide I region of the monomer, which was characteristic of the  $\text{NH}^+ \cdots \text{O}$  intramolecular interaction, is not observed here, which confirms the assignment.<sup>45</sup>

## Conclusion

The results presented here lead to the conclusion that the effects of stereochemistry on the protonated dimer of cyclo (Phe-His) strongly contrast with those observed in the protonated monomer. The c-(LL)H<sup>+</sup> and c-(LD)H<sup>+</sup> protonated monomers show identical structures, which cannot be distinguished by their vibrational spectroscopy in a room-temperature ion trap. However, they display very different CID efficiency, in particular for the CO loss channel, due to the shuttling mechanism of the proton localized on the imidazole.<sup>45</sup> In contrast, (c-LL)<sub>2</sub>H<sup>+</sup> and (c-LD)<sub>2</sub>H<sup>+</sup> have very different spectroscopic signatures that prove unambiguously that an antiparallel  $\beta$ -sheet interaction takes place in (c-LL)<sub>2</sub>H<sup>+</sup> and not in (c-LD)<sub>2</sub>H<sup>+</sup>. (c-LL)<sub>2</sub>H<sup>+</sup> and (c-LD)<sub>2</sub>H<sup>+</sup> differ much more in their spectroscopic signatures than systems showing a single strong interaction like a shared proton, as observed for example in the protonated alanine-camphor dimer, whose floppiness prevents the formation of stereoselective additional interaction points.<sup>84</sup> They also show much more specificity than chiral amino acids<sup>85</sup> like glutamic acid dimers or other simple systems like sodium core methyl tartrate dimers, although the latter display the multiple interaction points that are thought to be necessary for chiral recognition.<sup>86</sup> This selectivity probably arises partially from the diastereomerism being intramolecular in nature, in contrast to the diastereomeric complexes mentioned above, which might result in stronger effects due to reduced flexibility.<sup>61</sup> This may also be due to the peculiar properties of histidine. Indeed, the strong sensitivity to chirality observed here strongly contrasts with what is observed for the cyclo (Tyr-Pro) protonated dimer, the structure of which is identical for identical or opposite absolute configurations of the residues.<sup>46</sup> These results support the peculiar role of histidine in the structure and fragmentation of peptides.<sup>51,87</sup> The differences between (c-LL)<sub>2</sub>H<sup>+</sup> and (c-LD)<sub>2</sub>H<sup>+</sup> are very marked, and do not involve weak ancillary interactions as seen in other systems but the presence or not of an antiparallel  $\beta$ -sheet.<sup>61,88</sup> While  $\text{N}_\pi$  of the neutral part acts as an acceptor in the ionic  $\text{NH}^+ \cdots \text{N}$  hydrogen bond for both protonated dimers, as it does in neutral imidazole or His-containing peptides,<sup>77,79</sup> the two diastereomer differ in the nature of the  $\text{NH}^+$  group of the protonated moiety that acts as a donor. It is  $\text{N}_\text{t}\text{H}^+$  in (c-LD)<sub>2</sub>H<sup>+</sup> while it is  $\text{N}_\pi\text{H}^+$  for (c-LL)<sub>2</sub>H<sup>+</sup>. Last, the complexes observed in the ion trap are not the most stable calculated structures. Trapping higher energy conformers is frequently observed in experiments coupling mass spectrometry and laser spectroscopy and results from kinetic trapping of species entropically favoured at the high temperatures achieved during the electro-spray ionisation process.<sup>89-92</sup> It may result from a non-thermodynamic distribution of the electrospray due partly to the high but non-evaluatable temperature

and from the important role of the solvent in the aggregation process right before the vaporization. Continuum solvation models used in this work are not sufficient to account for the modification of relative energies by solvation. This point must be especially true in the case of histidine-containing peptides due to their large sensitivity to solvation and deserves further theoretical investigation.<sup>49</sup>

## Conflicts of interest

There are no conflict to declare.

## Acknowledgements

We thank Dr Ivan Alata for experimental assistance. We thank Dr D. Seuderi and the CLIO team for technical assistance and helpful discussions. We acknowledge the computing centre MesoLUM managed by ISMO (UMR8214) and LPGP (UMR8578), University Paris-Saclay (France). The research described here has been supported by the French National Research Agency (ANR; Grant ANR-17-CE29-0008 "TUNIFOLD-S").

## References

- 1 R. Nelson, M. R. Sawaya, M. Balbirnie, A. O. Madsen, C. Riekel, R. Grothe and D. Eisenberg, *Nature*, 2005, **435**, 773–778.
- 2 O. S. Makin and L. C. Serpell, *FEBS J.*, 2005, **272**, 5950–5961.
- 3 R. Gallardo, N. A. Ranson and S. E. Radford, *Curr. Opin. Struct. Biol.*, 2020, **60**, 7–16.
- 4 M. R. Sawaya, S. Sambashivan, R. Nelson, M. I. Ivanova, S. A. Sievers, M. I. Apostol, M. J. Thompson, M. Balbirnie, J. J. W. Wiltzius, H. T. McFarlane, A. O. Madsen, C. Riekel and D. Eisenberg, *Nature*, 2007, **447**, 453–457.
- 5 K. Schwing and M. Gerhards, *Int. Rev. Phys. Chem.*, 2016, **35**, 569–677.
- 6 E. Gloaguen, M. Mons, K. Schwing and M. Gerhards, *Chem. Rev.*, 2020, **120**, 12490–12562.
- 7 B. C. Dian, A. Longarte, S. Mercier, D. A. Evans, D. J. Wales and T. S. Zwier, *J. Chem. Phys.*, 2002, **117**, 10688–10702.
- 8 W. H. James, E. E. Baquero, S. H. Choi, S. H. Gellman and T. S. Zwier, *J. Phys. Chem. A*, 2010, **114**, 1581–1591.
- 9 J. R. Gord, P. S. Walsh, B. F. Fisher, S. H. Gellman and T. S. Zwier, *J. Phys. Chem. B*, 2014, **118**, 8246–8256.
- 10 M. Gerhards, C. Unterberg, A. Gerlach and A. Jansen, *Phys. Chem. Chem. Phys.*, 2004, **6**, 2682–2690.
- 11 H. Fricke, G. Schafer, T. Schrader and M. Gerhards, *Phys. Chem. Chem. Phys.*, 2007, **9**, 4592–4597.
- 12 E. Gloaguen and M. Mons, in *Gas-Phase IR Spectroscopy and Structure of Biological Molecules*, ed. A. M. Rijs and J. Oomens, 2015, vol. 364, pp. 225–270.
- 13 Y. Loquais, E. Gloaguen, S. Habka, V. Vaquero-Vara, V. Brenner, B. Tardivel and M. Mons, *J. Phys. Chem. A*, 2015, **119**, 5932–5941.



14 S. Chakraborty, K. Yamada, S. Ishiuchi and M. Fujii, *Chem. Phys. Lett.*, 2012, **531**, 41–45.

15 H. Otaki, K. Yagi, S. Ishiuchi, M. Fujii and Y. Sugita, *J. Phys. Chem. B*, 2016, **120**, 10199–10213.

16 A. Abo-Riziq, J. E. Bushnell, B. Crews, M. Callahan, L. Grace and M. S. De Vries, *Chem. Phys. Lett.*, 2006, **431**, 227–230.

17 A. Abo-Riziq, L. Grace, B. Crews, M. P. Callahan, T. van Mourik and M. S. D. Vries, *J. Phys. Chem. A*, 2011, **115**, 6077–6087.

18 J. A. Stearns, M. Guidi, O. V. Boyarkin and T. R. Rizzo, *J. Chem. Phys.*, 2007, **127**, 154322.

19 T. K. Roy, V. Kopysov, N. S. Nagornova, T. R. Rizzo, O. V. Boyarkin and R. B. Gerber, *ChemPhysChem*, 2015, **16**, 1374–1378.

20 R. C. Dunbar, G. Berden and J. Oomens, *Int. J. Mass Spectrom.*, 2013, **354–355**, 356–364.

21 R. C. Dunbar, J. Oomens, G. Berden, J. K.-C. Lau, U. H. Verkerk, A. C. Hopkinson and K. W. M. Siu, *J. Phys. Chem. A*, 2013, **117**, 5335–5343.

22 T. D. Vaden, S. A. N. Gowers, T. S. J. A. de Boer, J. D. Steill, J. Oomens and L. C. Snoek, *J. Am. Chem. Soc.*, 2008, **130**, 14640–14650.

23 W. H. James, III, E. G. Buchanan, L. Guo, S. H. Gellman and T. S. Zwier, *J. Phys. Chem. A*, 2011, **115**, 11960–11970.

24 R. Kusaka, D. Zhang, P. S. Walsh, J. R. Gord, B. F. Fisher, S. H. Gellman and T. S. Zwier, *J. Phys. Chem. A*, 2013, **117**, 10847–10862.

25 P. S. Walsh, R. Kusaka, E. G. Buchanan, W. H. James, III, B. F. Fisher, S. H. Gellman and T. S. Zwier, *J. Phys. Chem. A*, 2013, **117**, 12350–12362.

26 M. Alauddin, E. Gloaguen, V. Brenner, B. Tardivel, M. Mons, A. Zehnacker-Rentien, V. Declerck and D. J. Aitken, *Chem. – Eur. J.*, 2015, **21**, 16479–16493.

27 Z. Imani, V. R. Mundlapati, G. Goldsztejn, V. Brenner, E. Gloaguen, R. Guillot, J. P. Baltaze, K. Le Barbu-Debus, S. Robin, A. Zehnacker, M. Mons and D. J. Aitken, *Chem. Sci.*, 2020, **11**, 9191–9197.

28 V. R. Mundlapati, Z. Imani, G. Goldsztejn, E. Gloaguen, V. Brenner, K. Le Barbu-Debus, A. Zehnacker-Rentien, J. P. Baltaze, S. Robin, M. Mons and D. J. Aitken, *Amino Acids*, 2021, **53**, 621–633.

29 K. N. Blodgett, G. Jang, S. Kim, M. K. Kim, S. H. Choi and T. S. Zwier, *J. Phys. Chem. A*, 2020, **124**, 5856–5870.

30 V. Declerck, A. Pérez-Mellor, R. Guillot, D. J. Aitken, M. Mons and A. Zehnacker, *Chirality*, 2019, **31**, 547–560.

31 V. R. Mundlapati, Z. Imani, V. C. D'Mello, V. Brenner, E. Gloaguen, J. P. Baltaze, S. Robin, M. Mons and D. J. Aitken, *Chem. Sci.*, 2021, **12**, 14826–14832.

32 H. S. Biswal, Y. Loquais, B. Tardivel, E. Gloaguen and M. Mons, *J. Am. Chem. Soc.*, 2011, **133**, 3931–3942.

33 J. Ujma, V. Kopysov, N. S. Nagornova, L. G. Migas, M. G. Lizio, E. W. Blanch, C. MacPhee, O. V. Boyarkin and P. E. Barran, *Angew. Chem., Int. Ed.*, 2018, **57**, 213–217.

34 M. Gerhards and C. Unterberg, *Phys. Chem. Chem. Phys.*, 2002, **4**, 1760–1765.

35 J. Seo, W. Hoffmann, S. Warnke, X. Huang, S. Gewinner, W. Schollkopf, M. T. Bowers, G. von Helden and K. Pagel, *Nat. Chem.*, 2017, **9**, 39–44.

36 A. Pérez-Mellor, K. Le Barbu-Debus and A. Zehnacker, *Chirality*, 2020, **32**, 693–703.

37 A. Pérez-Mellor, I. Alata, V. Lepère and A. Zehnacker, *J. Phys. Chem. B*, 2019, **123**, 6023–6033.

38 A. Pérez Mellor and A. Zehnacker, in *Physical Chemistry of Cold Gas-Phase Functional Molecules and Clusters*, ed. T. Ebata and M. Fujii, Springer, Singapore, 2019, pp. 63–87.

39 A. Pérez-Mellor, I. Alata, V. Lepère and A. Zehnacker, *J. Mol. Spectrosc.*, 2018, **349**, 71–84.

40 F. BenNasr, A. Pérez-Mellor, I. Alata, V. Lepère, N. E. Jaidane and A. Zehnacker, *Faraday Discuss.*, 2018, **212**, 399–419.

41 A. Pérez-Mellor and A. Zehnacker, *Chirality*, 2017, **29**, 89–96.

42 P. T. Lansbury, P. R. Costa, J. M. Griffiths, E. J. Simon, M. Auger, K. J. Halverson, D. A. Kocisko, Z. S. Hendsch, T. T. Ashburn, R. G. S. Spencer, B. Tidor and R. G. Griffin, *Nat. Struct. Biol.*, 1995, **2**, 990–998.

43 S. Bakels, M. P. Gaigeot and A. M. Rijs, *Chem. Rev.*, 2020, **120**, 3233–3260.

44 M. Gdaniec and B. Liberek, *Acta Crystallogr., Sect. C: Cryst. Struct. Commun.*, 1986, **42**, 1343–1345.

45 A. Pérez-Mellor, K. Le Barbu-Debus, V. Lepère, I. Alata, R. Spezia and A. Zehnacker, *Eur. Phys. J. D*, 2021, **75**, 165.

46 A. Pérez-Mellor, I. Alata, V. Lepère, R. Spezia and A. Zehnacker-Rentien, *Int. J. Mass Spectrom.*, 2021, **465**, 116590.

47 A. Pérez Mellor and R. Spezia, *J. Chem. Phys.*, 2021, **155**, 124103.

48 M. Citir, C. S. Hinton, J. Oomens, J. D. Steill and P. B. Armentrout, *Int. J. Mass Spectrom.*, 2012, **330**, 6–15.

49 A. Y. Pereverzev, V. Kopysov and O. V. Boyarkin, *Angew. Chem., Int. Ed.*, 2017, **56**, 15639–15643.

50 G. Tsaprailis, H. Nair, W. Zhong, K. Kuppannan, J. H. Futrell and V. H. Wysocki, *Anal. Chem.*, 2004, **76**, 2083–2094.

51 A. C. Gucinski, J. Chamot-Rooke, E. Nicol, A. Somogyi and V. H. Wysocki, *J. Phys. Chem. A*, 2012, **116**, 4296–4304.

52 Y. Y. Huang, V. H. Wysocki, D. L. Tabb and J. R. Yates, *Int. J. Mass Spectrom.*, 2002, **219**, 233–244.

53 B. R. Perkins, J. Chamot-Rooke, S. H. Yoon, A. C. Gucinski, A. Somogyi and V. H. Wysocki, *J. Am. Chem. Soc.*, 2009, **131**, 17528–17529.

54 J. Cautereels, J. Giribaldi, C. Enjalbal and F. Blockhuys, *Rapid Commun. Mass Spectrom.*, 2020, **34**, e8778.

55 P. J. Milne, D. W. Oliver and H. M. Roos, *J. Crystallogr. Spectrosc. Res.*, 1992, **22**, 643–649.

56 P. Maitre, S. Le Caer, A. Simon, W. Jones, J. Lemaire, H. Mestdagh, M. Heninger, G. Mauclaire, P. Boissel, R. Prazeres, F. Glotin and J. M. Ortega, *Nucl. Instrum. Methods Phys. Res., Sect. A*, 2003, **507**, 541–546.

57 R. Prazeres, F. Glotin, C. Insa, D. A. Jaroszynski and J. M. Ortega, *Eur. Phys. J. D*, 1998, **3**, 87–93.

58 J. M. Bakker, T. Besson, J. Lemaire, D. Scuderi and P. Maitre, *J. Phys. Chem. A*, 2007, **111**, 13415–13424.

59 I. Alata, A. Pérez-Mellor, F. Ben Nasr, D. Scuderi, V. Steinmetz, F. Gobert, N. E. Jaidane and A. Zehnacker-Rentien, *J. Phys. Chem. A*, 2017, **121**, 7130–7138.

60 P. Maitre, D. Scuderi, D. Corinti, B. Chiavarino, M. E. Crestoni and S. Fornarini, *Chem. Rev.*, 2020, **120**, 3261–3295.



61 A. Zehnacker, *Int. Rev. Phys. Chem.*, 2014, **33**, 151–207.

62 N. C. Polfer, *Chem. Soc. Rev.*, 2011, **40**, 2211–2221.

63 *MacroModel version 9.8*, Schrödinger, LLC, New York, NY, 2010.

64 E. Harder, W. Damm, J. Maple, C. Wu, M. Reboul, J. Y. Xiang, L. Wang, D. Lupyán, M. K. Dahlgren, J. L. Knight, J. W. Kaus, D. S. Cerutti, G. Krilov, W. L. Jorgensen, R. Abel and R. A. Friesner, *J. Chem. Theory Comput.*, 2016, **12**, 281–296.

65 R. Ahlrichs, M. Bar, M. Haser, H. Horn and C. Kolmel, *Chem. Phys. Lett.*, 1989, **162**, 165–169.

66 *Turbomole V6.6 2014*, A development of University of Karlsruhe and Forschungszentrum Karlsruhe GmbH Turbomole GmbH, 2014.

67 A. D. Becke, *J. Chem. Phys.*, 1997, **107**, 8554–8560.

68 S. Grimme, J. Antony, S. Ehrlich and H. Krieg, *J. Chem. Phys.*, 2010, **132**, 154104.

69 D. Rappoport and F. Furche, *J. Chem. Phys.*, 2010, **133**, 134105.

70 F. Furche, R. Ahlrichs, C. Hättig, W. Klopper, M. Sierka and F. Weigend, *Wiley Interdiscip. Rev.: Comput. Mol. Sci.*, 2014, **4**, 91–100.

71 L. Goerigk and S. Grimme, *Phys. Chem. Chem. Phys.*, 2011, **13**, 6670–6688.

72 A. D. Becke, *Phys. Rev. A: At., Mol., Opt. Phys.*, 1988, **38**, 3098–3100.

73 M. D. Halls, J. Velkovski and H. B. Schlegel, *Theor. Chem. Acc.*, 2001, **105**, 413.

74 M. J. Frisch, J. A. Pople and J. S. Binkley, *J. Chem. Phys.*, 1984, **80**, 3265–3269.

75 M. J. Frisch, G. W. Trucks, H. B. Schlegel, G. E. Scuseria, M. A. Robb, J. R. Cheeseman, G. Scalmani, V. Barone, G. A. Petersson, H. Nakatsuji, X. Li, M. Caricato, A. V. Marenich, J. Bloino, B. G. Janesko, R. Gomperts, B. Mennucci, H. P. Hratchian, J. V. Ortiz, A. F. Izmaylov, J. L. Sonnenberg, D. Williams-Young, F. Ding, F. Lipparini, F. Egidi, J. Goings, B. Peng, A. Petrone, T. Henderson, D. Ranasinghe, V. G. Zakrzewski, J. Gao, N. Rega, G. Zheng, W. Liang, M. Hada, M. Ehara, K. Toyota, R. Fukuda, J. Hasegawa, M. Ishida, T. Nakajima, Y. Honda, O. Kitao, H. Nakai, T. Vreven, K. Throssell, J. A. Montgomery Jr., J. E. Peralta, F. Ogliaro, M. J. Bearpark, J. J. Heyd, E. N. Brothers, K. N. Kudin, V. N. Staroverov, T. A. Keith, R. Kobayashi, J. Normand, K. Raghavachari, A. P. Rendell, J. C. Burant, S. S. Iyengar, J. Tomasi, M. Cossi, J. M. Millam, M. Klene, C. Adamo, R. Cammi, J. W. Ochterski, R. L. Martin, K. Morokuma, O. Farkas, J. B. Foresman and D. J. Fox, *Gaussian 16, Revision B.01*, 2016.

76 C. P. McNary, Y. W. Nei, P. Maitre, M. T. Rodgers and P. B. Armentrout, *Phys. Chem. Chem. Phys.*, 2019, **21**, 12625–12639.

77 C. Bermudez, S. Mata, C. Cabezas and J. L. Alonso, *Angew. Chem., Int. Ed.*, 2014, **53**, 11015–11018.

78 S. Bakels, I. Stroganova and A. M. Rijs, *Phys. Chem. Chem. Phys.*, 2021, **23**, 20945–20956.

79 W. Y. Sohn, S. Habka, E. Gloaguen and M. Mons, *Phys. Chem. Chem. Phys.*, 2017, **19**, 17128–17142.

80 M. Y. Choi and R. E. Miller, *J. Phys. Chem. A*, 2006, **110**, 9344–9351.

81 S. Kumar, A. Mukherjee and A. Das, *J. Phys. Chem. A*, 2012, **116**, 11573–11580.

82 A. Bhattacharjee and S. Wategaonkar, *Phys. Chem. Chem. Phys.*, 2015, **17**, 20080–20092.

83 M. A. Trachsel, P. Ottigeri, H. M. Frey, C. Pfaffen, A. Bihlmeier, W. Klopper and S. Leutwyler, *J. Phys. Chem. B*, 2015, **119**, 7778–7790.

84 A. Sen, K. Le Barbu-Debus, D. Scuderi and A. Zehnacker-Rentien, *Chirality*, 2013, **25**, 436–443.

85 M. Poline, O. Rebrov, M. Larsson and V. Zhaunerchyk, *Chirality*, 2020, **32**, 359–369.

86 K. Le Barbu-Debus, D. Scuderi, V. Lepere and A. Zehnacker, *J. Mol. Struct.*, 2020, **1205**, 127583.

87 F. Turecek, T. W. Chung, C. L. Moss, J. A. Wyer, A. Ehlerding, A. I. S. Holm, H. Zettergren, S. B. Nielsen, P. Hvelplund, J. Chamot-Rooke, B. Bythell and B. Paizs, *J. Am. Chem. Soc.*, 2010, **132**, 10728–10740.

88 D. Scuderi, K. Le Barbu-Debus and A. Zehnacker, *Phys. Chem. Chem. Phys.*, 2011, **13**, 17916–17929.

89 S. S. Lee, J. U. Lee, J. H. Oh, S. Park, Y. Hong, B. K. Min, H. H. L. Lee, H. I. Kim, X. L. Kong, S. Lee and H. B. Oh, *Phys. Chem. Chem. Phys.*, 2018, **20**, 30428–30436.

90 L. Voronina and T. R. Rizzo, *Phys. Chem. Chem. Phys.*, 2015, **17**, 25828–25836.

91 E. Bodo, A. Ciavardini, A. Giardini, A. Paladini, S. Piccirillo, F. Rondino and D. Scuderi, *Chem. Phys.*, 2012, **398**, 124–128.

92 K. Hirata, Y. Mori, S. I. Ishiuchi, M. Fujii and A. Zehnacker, *Phys. Chem. Chem. Phys.*, 2020, **22**, 24887–24894.

